Supplementary Information

Ultrafast Synthesis of Porous Fe₃C/Carbon Hybrid Materials via Carbothermal Shock Reactor for Advanced Energy Storage Applications

Jun Cao[a], Kai-Yue Ji[a], Ming-He Du[a], Chi Zhang[b], Qi Sun[c], Ying Yi[d], Ze-Fan Chai[a], Chun-Jie Yan[a], Heng Deng[a,e,]*

[a] Faculty of Materials Science and Chemistry, China University of Geosciences, Wuhan, 430074, People's Republic of China

[b] Hangzhou Institute for Advanced Study, University of Chinese Academy of Sciences, Hangzhou 310024, People's Republic of China

[c] College of Materials and Metallurgy, Guizhou University, Guiyang 550025, People's Republic of China

[d] School of Mechanical Engineering and Electronic Information, China University of Geosciences, Wuhan, 430074, People's Republic of China

[e] Shenzhen Research Institute, China University of Geosciences, Shenzhen, 518000, People's Republic of China

*Corresponding author. dengheng@cug.edu.cn (Heng Deng).

Supplementary Text

Electrochemical test of SCs and MSCs: A three-electrode configuration was employed to assess the electrochemical performance of the SC samples. The working electrodes consisted of the as-prepared materials, platinum foils served as counter electrodes, and Hg/HgO electrodes were utilized as reference electrodes. Cyclic voltammetry (CV) and constant-current charge/discharge (GCD) measurements were conducted in 1 M KOH aqueous solution using a Shanghai Chenhua CHI 760E electrochemical workstation. The scanning rate for the CV test ranged from 50 to 1 mV s^{-1}, while the current density for the GCD test ranged from 6.0 to 0.5 A g^{-1}. Electrochemical impedance spectroscopy (EIS) testing was conducted at open circuit potential with a frequency range spanning from 0.1 to 10^5 Hz. The cyclic stability test of MSC is carried out under floating test, and the specific test process is as follows: Firstly, five GCD cycles were performed at 0.5 A g^{-1} within the electrochemical window of 0–1.0 V to estimate the supercapacitor capacity. After completing the cycling steps, a floating test was conducted with a maximum voltage (U_{max}) of 1.0 V.

For as-prepared SCs or MSC, we also used CV and GCD to evaluate their electrochemical performance. These tests were also performed by Chenhua CHI 760E electrochemical workstation. In general, the scan rate for the CV test and the current density for the GCD test were 50 ~ 1 mV s^{-1} and 6.0 ~ 0.5 A g^{-1}, respectively. The specific capacitance Cg (F g^{-1}) and area capacitance Cs (mF cm^{-2}) of as-prepared SCs or MSCs were calculated from GCD curves using the following equations:

$$C_M = \frac{I\Delta t}{M\Delta V} \tag{S1}$$

$$C_A = \frac{I\Delta t}{A\Delta V} \tag{S2}$$

where *M* stands the total mass of the effective part of electrodes, and *I* represents the current in the GCD test. The Δt represents the discharge time. The *A* represents the effective area for SCs or MSC. The energy density E and power density P of SCs or MSC can be calculated according to the following equations. The E_M and E_A represent for specific gravimetric energy density and specific areal energy density respectively. The P_M and P_A represent the specific gravimetric power density and specific areal power density, respectively.

$$E_M = \frac{\int_{t_1}^{t_2} V dt}{M3600}$$ (S3)

$$E_A = \frac{\int_{t_1}^{t_2} V dt}{A3600}$$ (S4)

$$P_M = \frac{E_M}{\Delta t}3600$$ (S5)

$$P_A = \frac{E_A}{\Delta t}3600$$ (S6)

To further understand the charge storage mechanism, the reaction kinetics of all samples were studied by CV profiles according to power law:

$$i = av^b$$ (S7)

Here, i and v represent the peak current response (A) and scan rate (V s^{-1}), a and b are computational parameters determined from the intercept and slope of the fit line of log(i) vs.log(v). Typically, b value close to 1 indicates a capacitive behavior that is dominated by the surface kinetic reaction, while b value equal to 0.5 signifies a battery-type property that is controlled by the diffusion process.

The quantitative kinetic analyses of all samples were performed according to Dunn's method:

$$i = k_1 v + k_2 v^{\frac{1}{2}}$$ (S8)

where i(V), $k_1 v$, and $k_2 v$ denote the total current response at a fixed potential V, current caused by surface capacitive effects, and current related to diffusion-controlled ion insertion process, respectively. Thus, by plotting i(V)/v$^{1/2}$ vs. v$^{1/2}$ at different potential windows, we can determine the values of k_1 and k_2 according to the slopes and

intercepts of the straight lines.

Electrochemical test of LIBs: Li-ion batteries (LIBs) were assembled in a glove box with argon filled (both H_2O and O_2<0.1 ppm). The as-prepared samples as work electrodes, Crade GF/D as separator and lithium foil were adopted as counter electrode, and 1 M LiPF6 in EC and DEC (1:1 by volume) as electrolyte. The assembled coin cells were GCD measured at various current densities in the potentials range of 0.01~3.0 V. CV was carried out on a Chenhua CHI 760E electrochemical workstation from 0.05 to 0.3 mV s^{-1} in a voltage range of 0~3.0 V. Electrochemical workstation was performed to collect the Electrochemical impedance spectroscopy (EIS) result in the frequency range of 0.1-10^5 Hz.
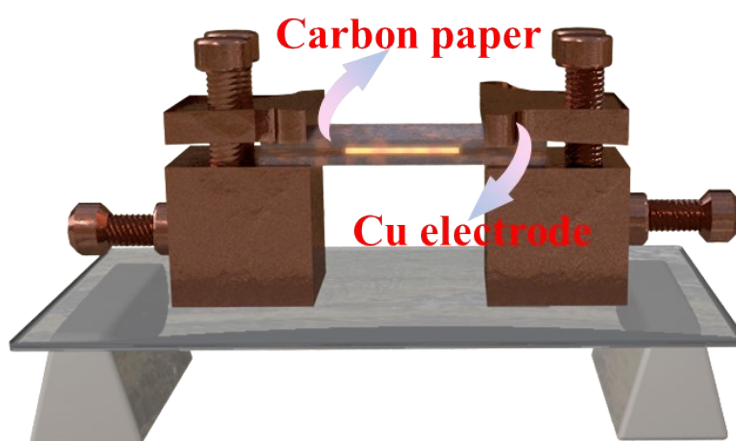
Fig. S1 The structure of CTS reactor.
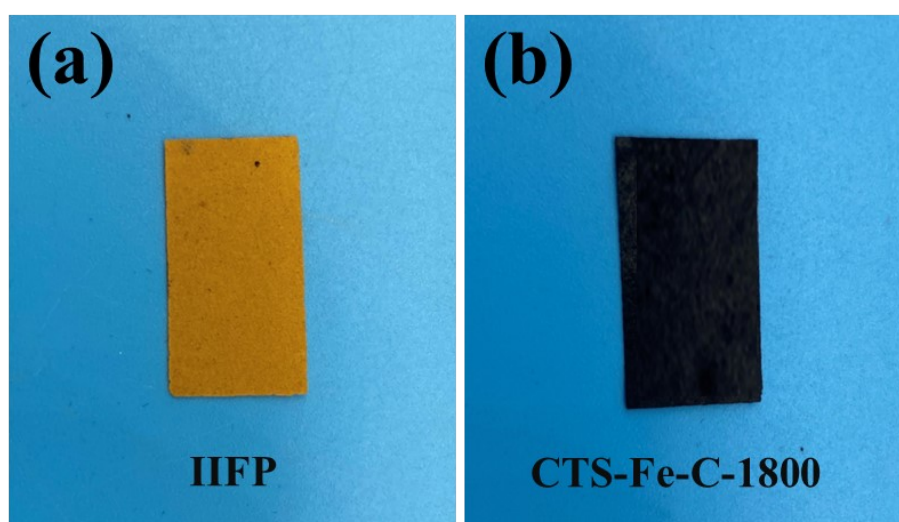
Fig. S2 (a, b) Optical images of IIFP and CTS-Fe-C-1800.
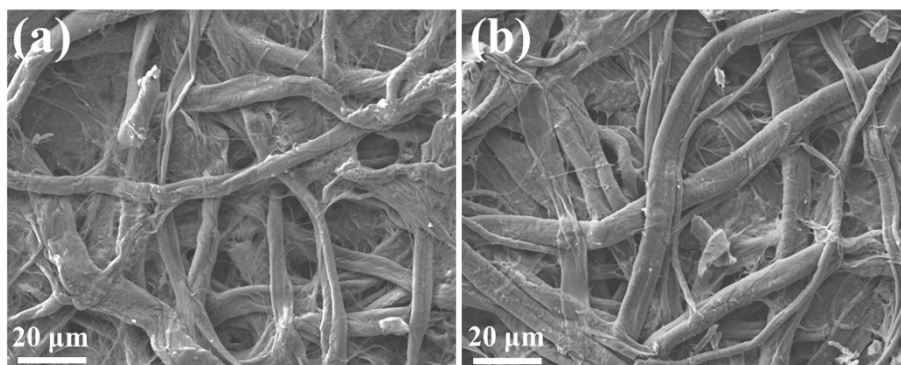
Fig. S3 (a, b) SEM images of filter paper (FP) and iron-impregnated filter paper (IIFP).
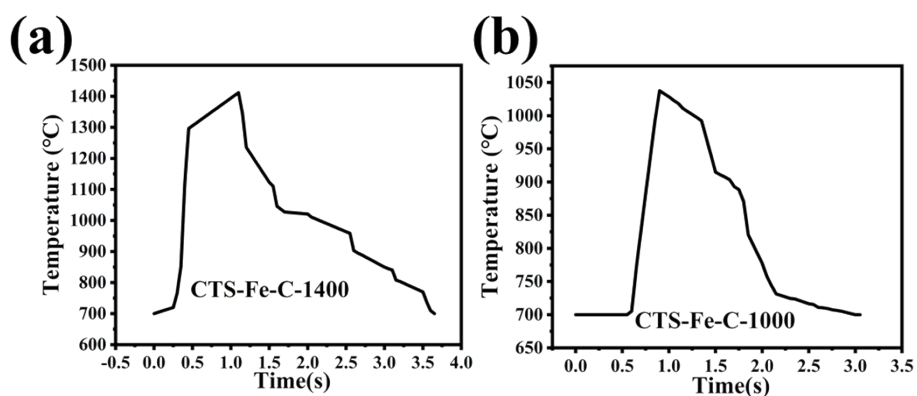
Fig. S4 (a, b) Temperature curves of CTS-Fe-C-1400 and CTS-Fe-C-1000 prepared by CTS reactor.
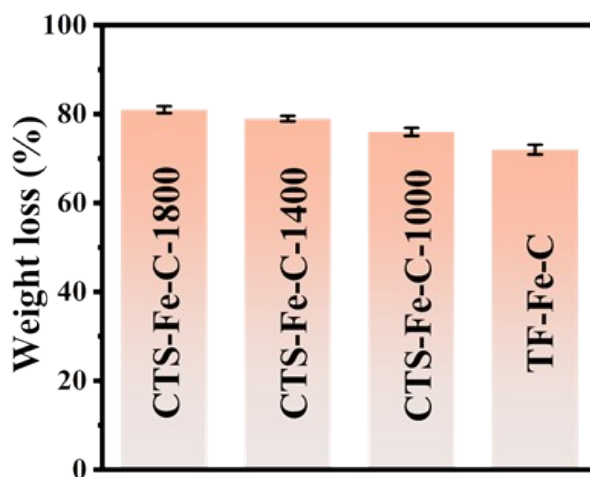
Fig. S5 Mass loss in the formation process of Fe-C samples.
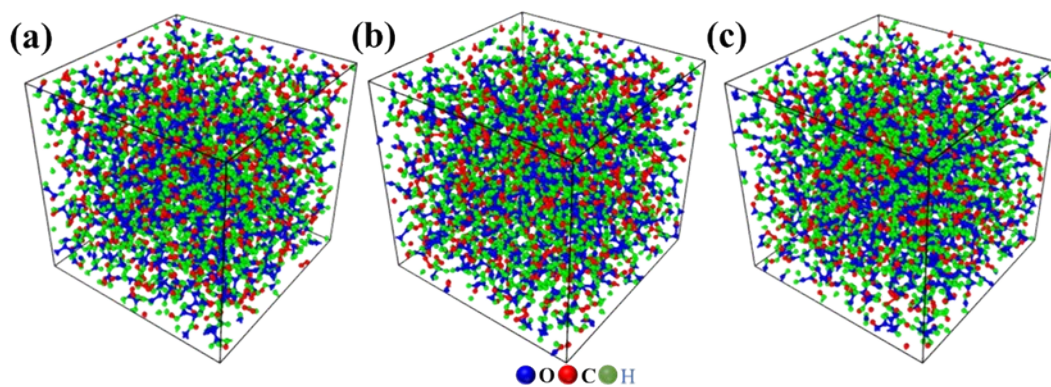
Fig. S6 (a-c) The results of the total pyrolysis products of CTS-Fe-C-1800, CTS-Fe-C-1400, and CTS-Fe-C-1000 prepared by CTS reactor.
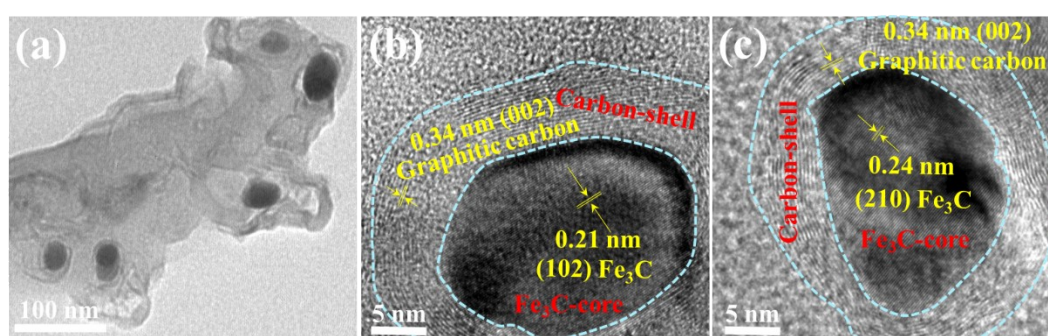
Fig. S7 (a) TEM image of CTS-Fe-C-1800, (b, c) HR-TEM images of CTS-Fe-C-1800.
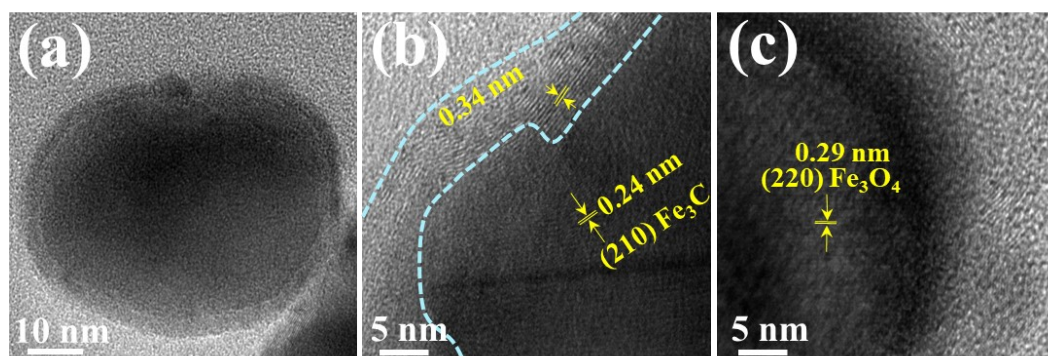
Fig. S8 (a) TEM image of CTS-Fe-C-1400, (b, c) HR-TEM images of CTS-Fe-C-1400.
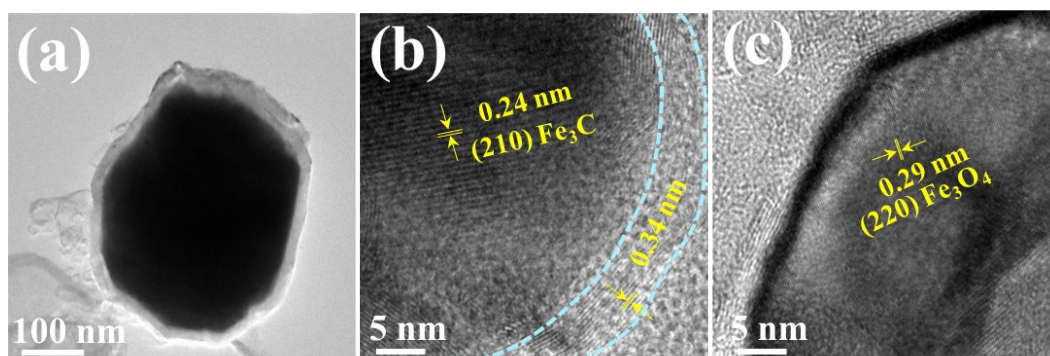
Fig. S9 (a) TEM image of CTS-Fe-C-1000, (b, c) HR-TEM images of CTS-Fe-C-1000.
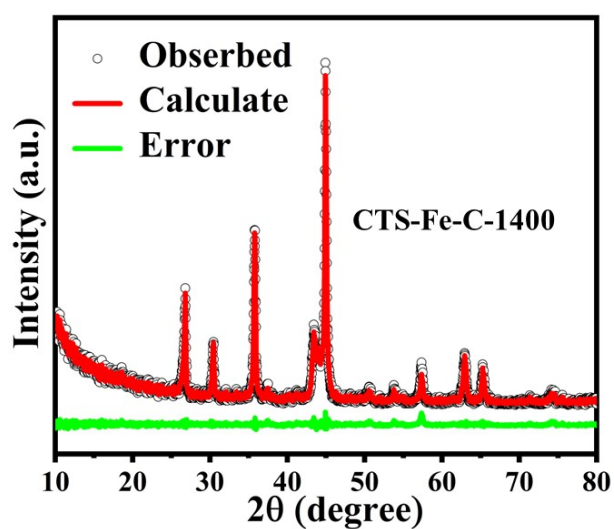
Fig. S10 XRD patterns Rietveld refinement of CTS-Fe-C-1400.
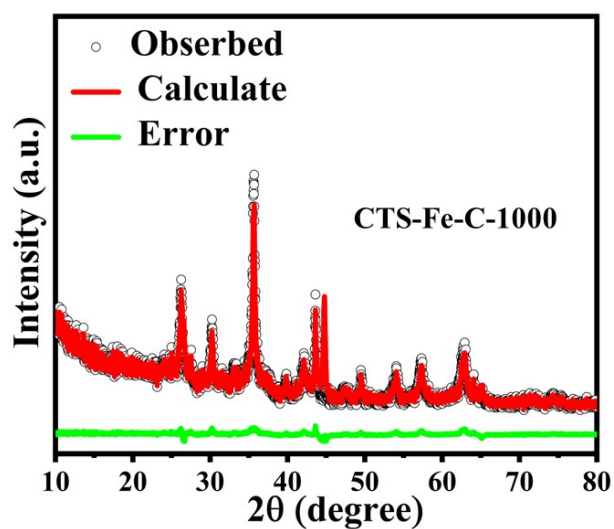
Fig. S11 XRD patterns Rietveld refinement of CTS-Fe-C-1000.

Calculation: The contents of carbon, Fe_3O_4, and Fe_3C in the Fe-C hybrids are

confirmed with Rietveld refinement of the XRD data and TG in the air from 25 °C to 900 °C.

$$4Fe_3C + 13O_2 = 6Fe_2O_3 + 4CO_2 \tag{S9}$$
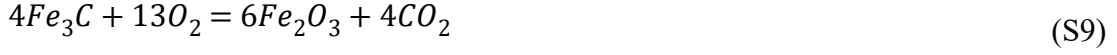
$$m_{Fe\,element}(\%) = m_{Fe2O3}(\%) \times \frac{2M_{Fe}}{M_{Fe2O3}} \tag{S10}$$

$$m_{Fe_3C}(\%) = m_{Fe\,element}(\%) \times \frac{M_{Fe_3C}}{3Fe} \tag{S11}$$

$$m_{Fe3O4}(\%) = \frac{m_{Fe\,element}(\%) \times \frac{M_{Fe3O4}}{3Fe}}{} \tag{S12}$$

$m_{Fe\,element}(\%)$ is the mass percentage of Fe element in Fe-C hybrids. $m_{Fe_3C}(\%)$ is the mass percentage of Fe_3C in Fe-C hybrids. $m_{Fe3O4}(\%)$ is the mass percentage of Fe_3O_4 in Fe-C hybrids. M_{Fe}, M_O, M_{Fe2O3}, M_{Fe3O4}, and M_{Fe_3C} are the molar masses of Fe, O, Fe_2O_3, Fe_3O_4, and Fe_3C.

For CTS-Fe-C-1800: Via TG, where of 69.8 wt. % is the weight of $m_{Fe2O3}(\%)$. So, $m_{Fe\,element}(\%)$ is 48.9 wt. %, as calculated based on equation (10). $m_{Fe_3C}(\%)$ is 52.4 wt. %, as calculated based on equation (11). $m_C(\%)$ is (100 wt. %-$m_{Fe_3C}(\%) =$ 100 wt. %-52.4 wt. %) 47.6 wt. %.

For CTS-Fe-C-1400: Via TG, where of 70 wt. % is the weight of $m_{Fe2O3}(\%)$. So, $m_{Fe\,element}(\%)$ is 49 wt. %, as calculated based on equation (10). According to Rietveld refinement of the XRD data, $m_{Fe3O4}(\%)$:$m_{Fe_3C}(\%)$=1.3. $m_{Fe_3C}(\%)$ is 26.2 wt. %. $m_{Fe3O4}(\%)$ is 34.1 wt. %. $m_C(\%)$ is 39.7 wt. %.

For CTS-Fe-C-1000: Via TG, where of 70.2 wt. % is the weight of $m_{Fe2O3}(\%)$. So, $m_{Fe\,element}(\%)$ is 49.1 wt. %, as calculated based on equation (10). According to

Rietveld refinement of the XRD data, $m_{Fe3O4}(\%):m_{Fe_3C}(\%)$ =3.2. $m_{Fe_3C}(\%)$ is 15.1 wt. %. $m_{Fe3O4}(\%)$ is 48.3 wt. %. $m_C(\%)$ is 36.6 wt. %.

For TF-Fe-C: Via TG, where of 69.7 wt. % is the weight of $m_{Fe2O3}(\%)$. So, $m_{Fe\ element}(\%)$ is 48.8 wt. %, as calculated based on equation (10). $m_{Fe_3O4}(\%)$ is 67.4 wt. %, as calculated based on equation (12). $m_C(\%)$ is (100 wt. %- $m_{Fe_3O4}(\%) =$ 100 wt. %-67.4 wt. %) 32.6 wt. %.
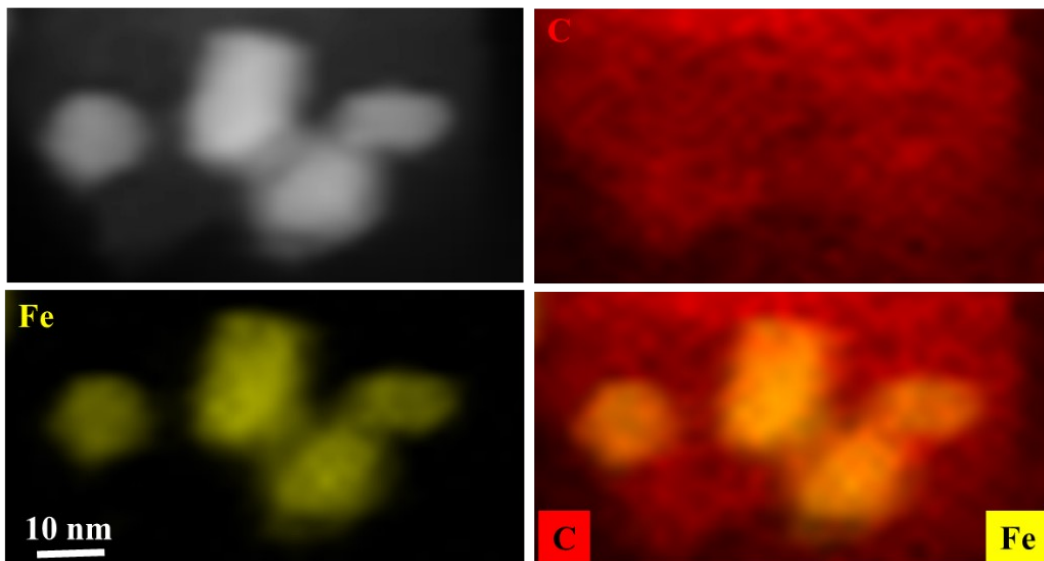
Fig. S12 TEM-mapping of CTS-Fe-C-1800.
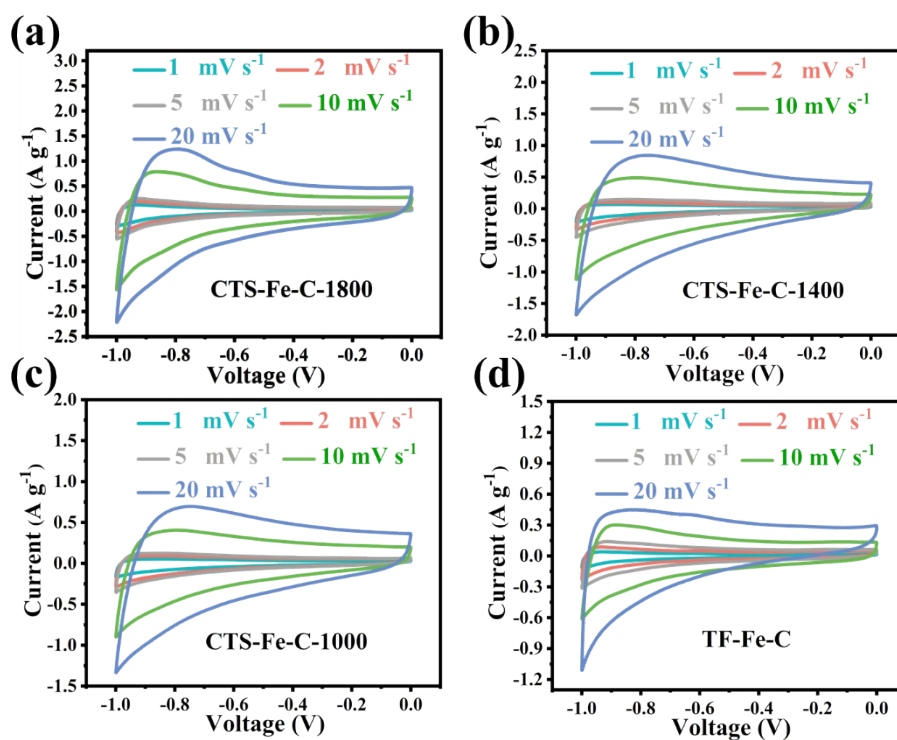
Fig. S13 (a-d) CV curves of CTS-Fe-C-1800, CTS-Fe-C-1400, CTS-Fe-C-1000, and TF-Fe-C SCs at different scan rates.
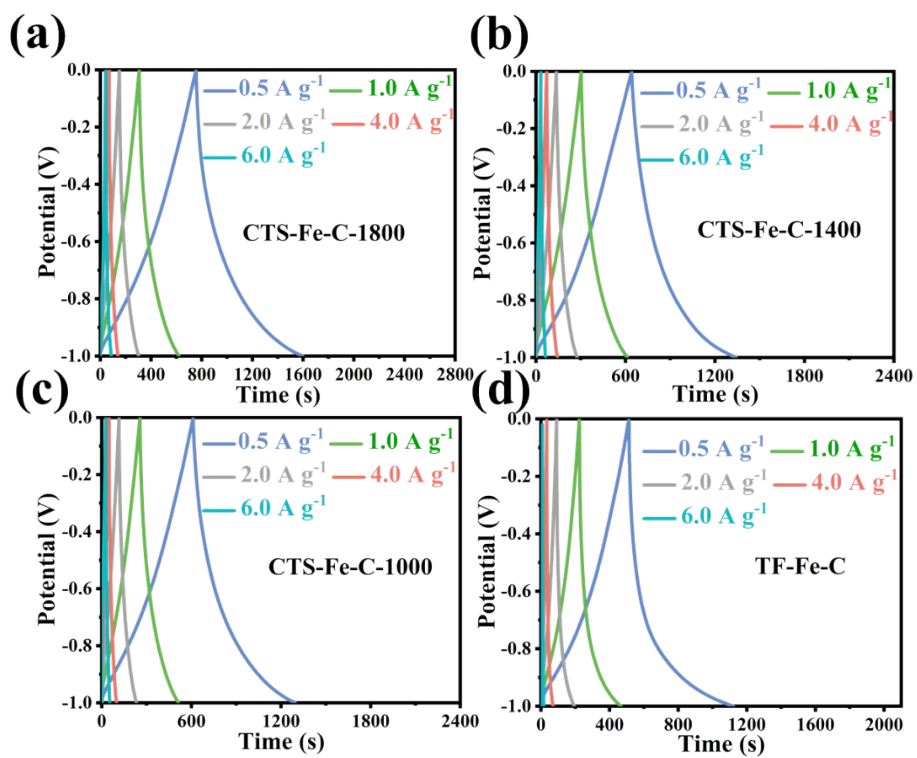
Fig. S14 (a-d) GCD curves of CTS-Fe-C-1800, CTS-Fe-C-1400, CTS-Fe-C-1000, and TF-Fe-C SCs at different current densities.
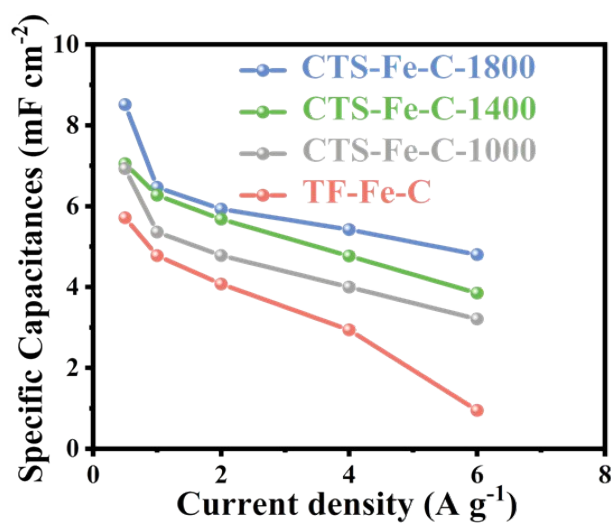
Fig. S15 Specific area capacitance of CTS-Fe-C-1800, CTS-Fe-C-1400, CTS-Fe-C-1000, and TF-Fe-C SCs at different current densities.
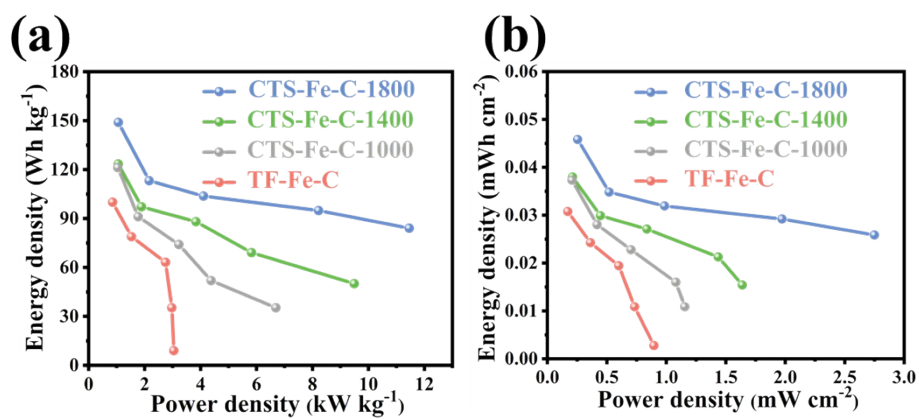
Fig. S16 (a, b) Ragone diagrams of CTS-Fe-C-1800, CTS-Fe-C-1400, CTS-Fe-C-1000, and TF-Fe-C SCs.
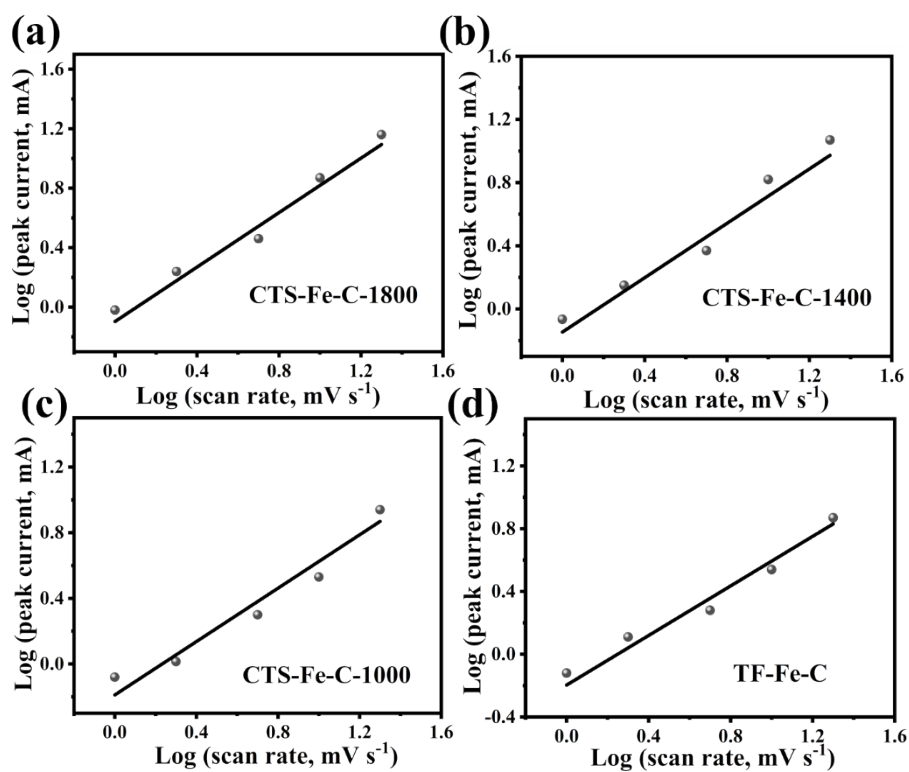
Fig. S17 (a-d) Log i vs log v plots of CTS-Fe-C-1800, CTS-Fe-C-1400, CTS-Fe-C-1000, and TF-Fe-C SCs.
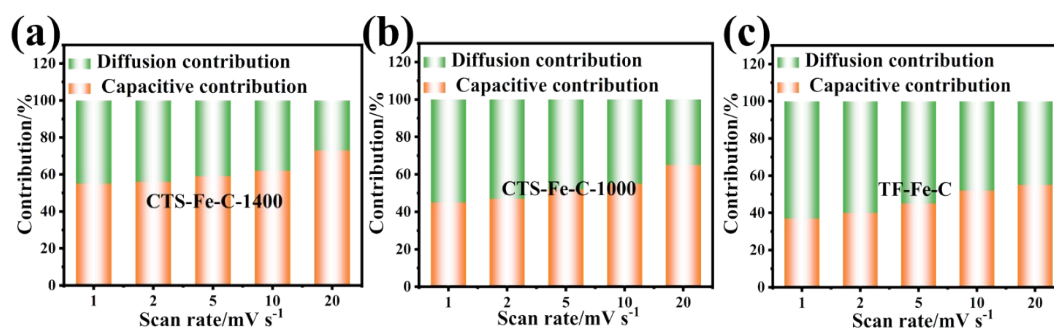
Fig. S18 (a-c) Contribution percentages of the capacitive and diffusion-controlled process at different scan rates of CTS-Fe-C-1400, CTS-Fe-C-1000, and TF-Fe-C SCs.
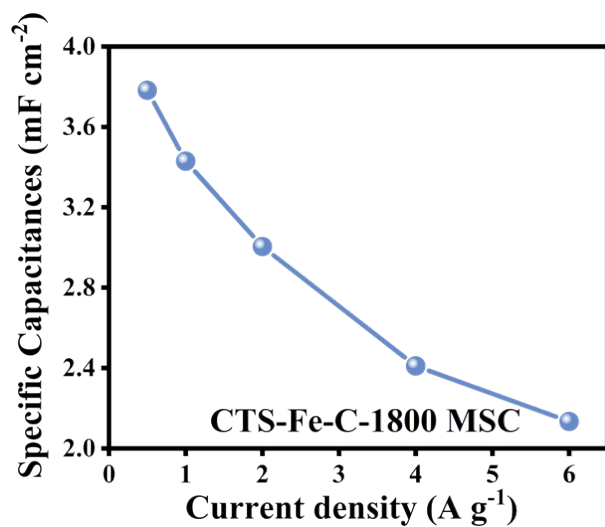
Fig. S19 Specific area capacitance of CTS-Fe-C-1800 MSC.
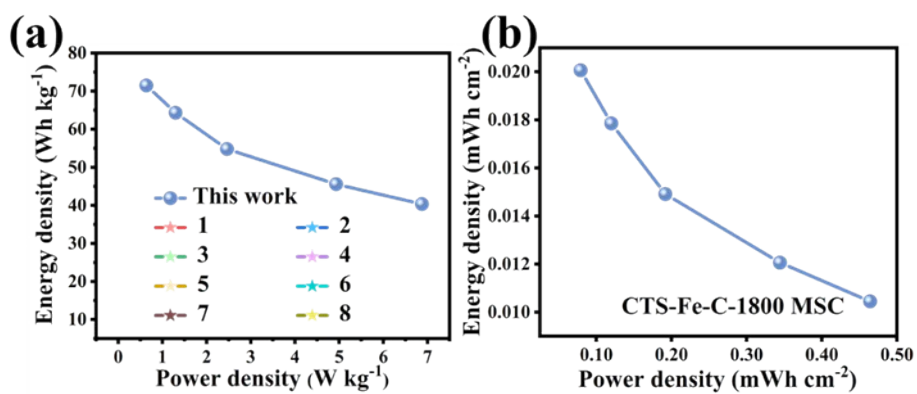
Fig. S20 (a, b) Ragone diagrams of CTS-Fe-C-1800 MSC [1-8].
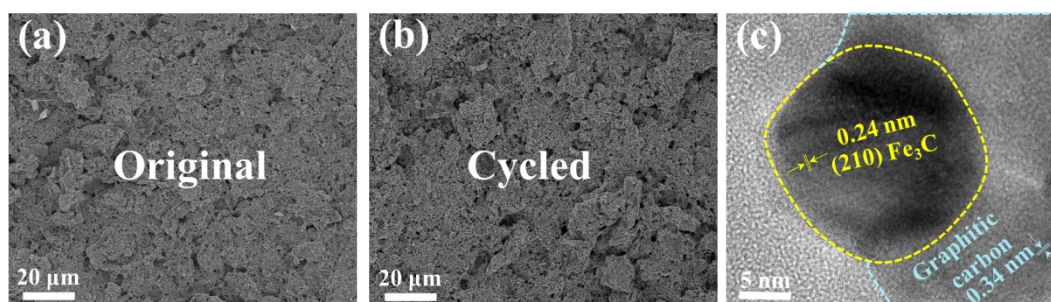
Fig. S21 (a, b) Original and cycled SEM images of CTS-Fe-C-1800 electrode in MSC. (c) TEM image of cycled CTS-Fe-C-1800 in MSC.
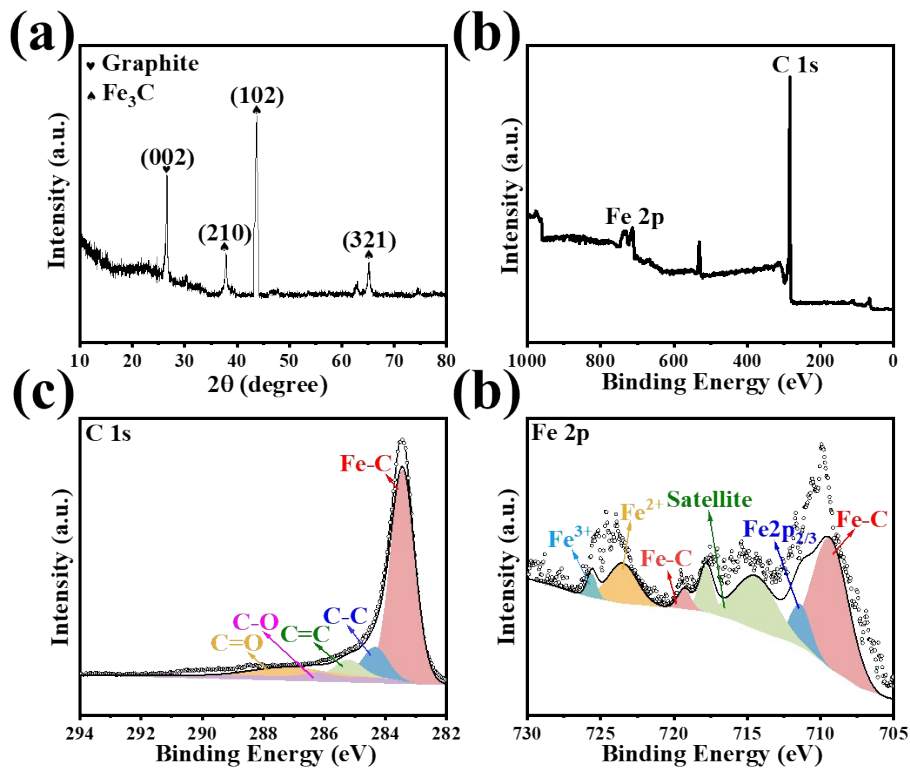
Fig. S22 (a) XRD pattern of the cycled CTS-Fe-C-1800 electrode in MSC. (b) XPS survey of the cycled CTS-Fe-C-1800 electrode in MSC. (c, d) High-resolution XPS surveys of C 1s and Fe 2p, respectively.
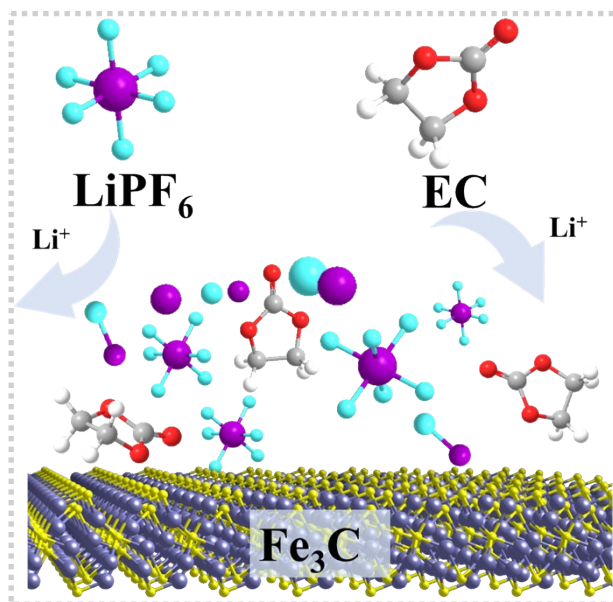
Fig. S23 Schematics of the SEI catalyzed by Fe_3C.
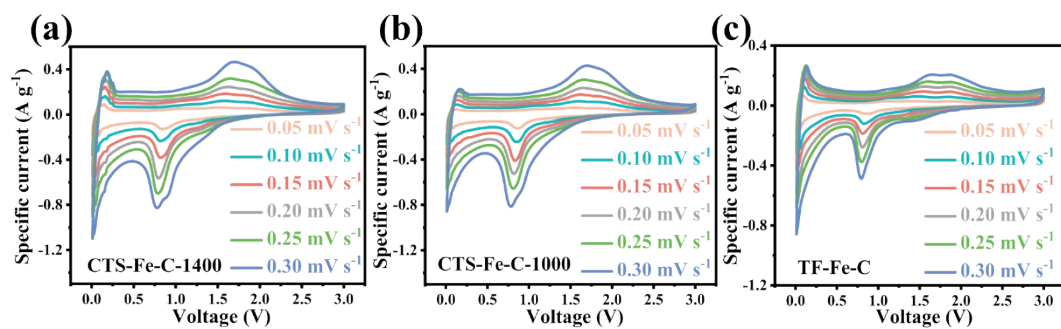
Fig. S24 (a-c) CV curves of CTS-Fe-C-1400, CTS-Fe-C-1000, and TF-Fe-C LIBs at different scan rates.
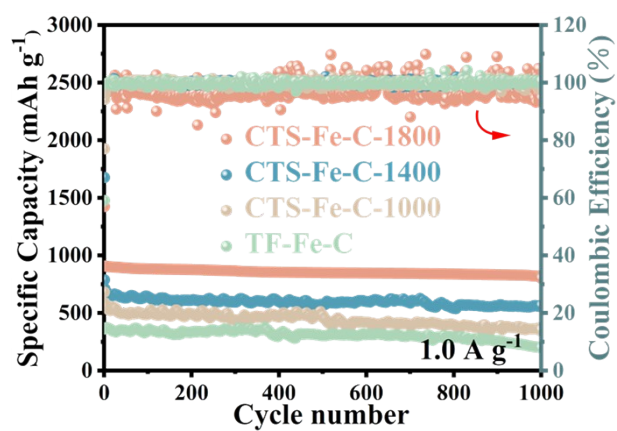
Fig. S25 Cycling performance of CTS-Fe-C-1800, CTS-Fe-C-1400, CTS-Fe-C-1000, and TF-Fe-C LIBs at 1.0 A g^{-1}.
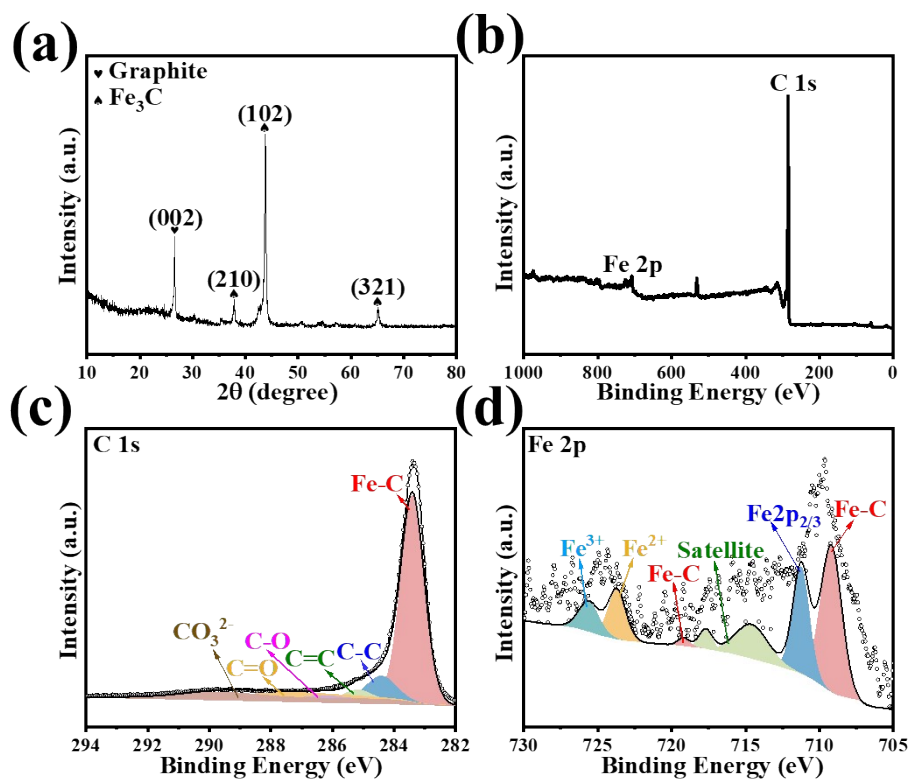
Fig. S26 (a) XRD pattern of the cycled CTS-Fe-C-1800 electrode in LIB. (b) XPS survey of the cycled CTS-Fe-C-1800 electrode in LIB (c, d) High-resolution XPS surveys of C 1s and Fe 2p, respectively.
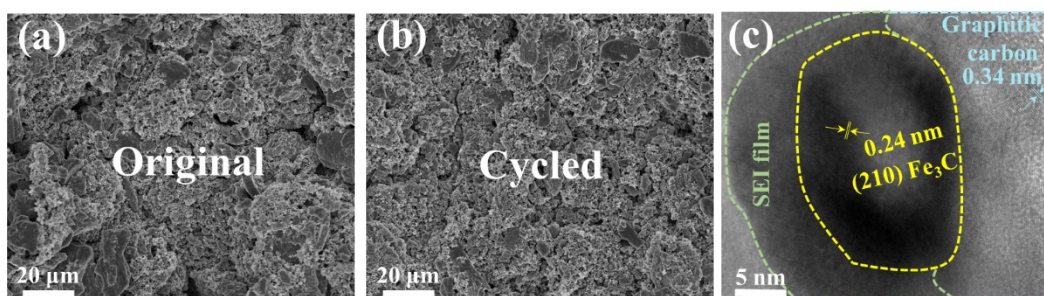
Fig. S27 (a, b) Original and cycled SEM images of CTS-Fe-C-1800 electrode in LIB. (c) TEM image of cycled CTS-Fe-C-1800 in LIB.
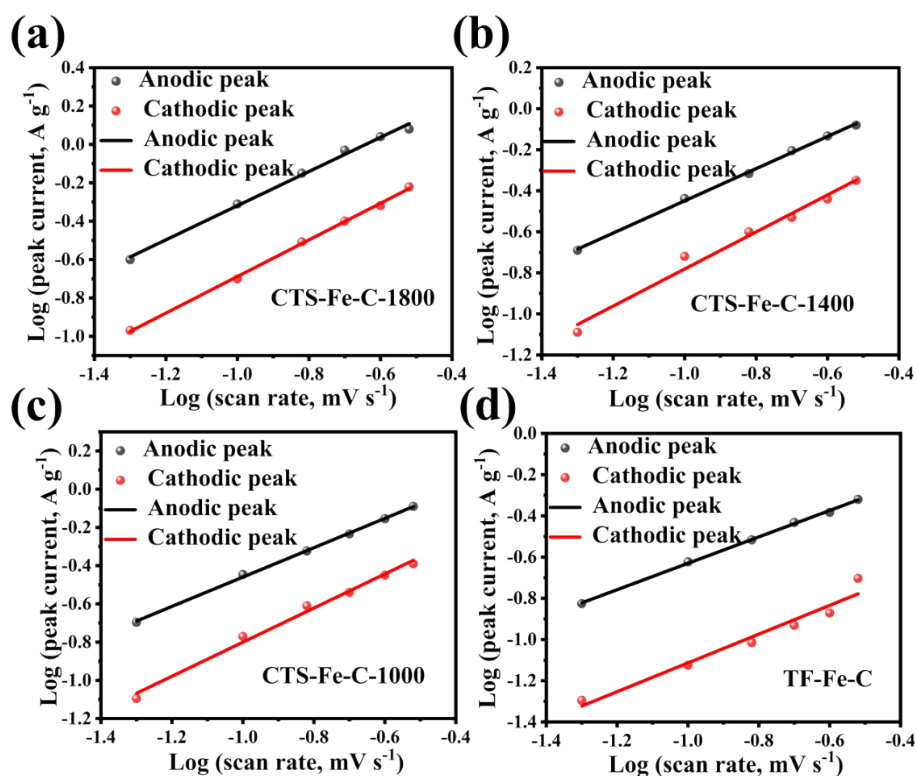
Fig. S28 (a-d) Log i vs log v plots of CTS-Fe-C-1800, CTS-Fe-C-1400, CTS-Fe-C-1000, and TF-Fe-C LIBs at different scan rates.
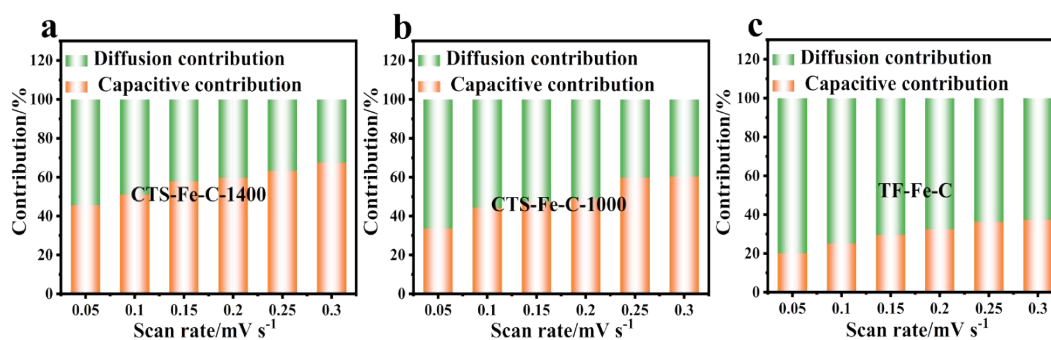
Fig. S29 (a-c) Contribution percentages of the capacitive and diffusion-controlled process at different scan rates of CTS-Fe-C-1400, CTS-Fe-C-1000, and TF-Fe-C LIBs.

Table S1. The surface area of CTS-Fe-C-1800, CTS-Fe-C-1400, CTS-Fe-C-1000, and TF-Fe-C.

Samples	BET Surface Area (m^2 g^{-1})
CTS-Fe-C-1800	161.3
CTS-Fe-C-1400	118.1
CTS-Fe-C-1000	35
TF-Fe-C	5.8

Table S2. Performance summary of Fe_3C-based SCs.

Electrode	Specific capacity (F g^{-1})	Electrolyte	References
Hierarchical porous N-doped carbon with Fe/Fe_3C	246	6 M KOH	9
Carbon encapsulated Fe/Fe_3C	223	1 M KOH	10
CTS-Fe-C-1800	323.3	1 M KOH	This work
Fe_3O_4/Fe_3C@N-doped carbon	217.8	6 M KOH	11
Fe_3C@CNF-650	205	6 M KOH	12

Table S3. Performance summary of Fe_3C-based MSCs.

Electrode	Energy density (Wh kg^{-1})	Electrolyte	References
Fe_3C/Fe_2O_3-anchored N-doped ECNF	14.2	1 M KOH/PVA	13
C-Fe/PANI	41.3	1 M KOH/PVA	14
CTS-Fe-C-1800	71.49	1 M KOH/PVA	This work
Fe_3O_4/Fe_3C@N-doped carbon	68	0.5 M Li_2SO_4	15
Fe_2O_3/NPC@Fe_3C/EPCNFs	21.6	1 M KOH/PVA	16

Table S4. Performance summary of Fe-based carbon anode for LIBs.

Electrode	Current density	Reversible capacity (mAh g^{-1})	References
Sn–Fe–C	1.0 A g^{-1}	537	**17**
Sn–Fe@C	1.0 A g^{-1}	439	**18**
Fe$_3$SnC@CNF	1.0 A g^{-1}	543	**19**
Fe$_3$O$_4$/C@VOx	1.0 A g^{-1}	605	**20**
UTS-Fe$_3$C/C-1800	1.0 A g^{-1}	801	**This work**
Fe$_2$Zn$_3$S$_5$/Fe$_x$S@C	0.5 A g^{-1}	622	**21**
Fe$_3$C/APCM	1.0 A g^{-1}	185	**22**
Fe$_3$C-carbon	0.2 A g^{-1}	197	**23**
Carbon-coated α-Fe$_2$O$_3$@Fe$_3$O$_4$	1.0 A g^{-1}	498	**24**

References

1. A. K. Das, E. G. Shankar, B. Ramulu and J. S. Yu, *Chem. Eng. J*, 2022, **448**, 137725.
2. F. Wang, T. Wang, S. Sun, Y. Xu, R. Yu and H. Li, *Sci. Rep*, 2018, **8**, 8908.
3. B. Ding, D. Guo, Y. Wang, X. Wu and Z. Fan, *J. Power Sources*, 2018, **398**, 113-119.
4. B. Ding and X. Wu, *J. Alloys Compd*, 2020, **842**, 155838.
5. C. Li, S. Wang, Y. Cui, X. Wang, Z. Yong, D. Liang, Y. Chi and Z. Wang, *ACS Appl. Mater*, 2022, **14**, 9172-9182.
6. K. O. Oyedotun, T. M. Masikhwa, A. A. Mirghni, B. K. Mutuma and N. Manyala, *Electrochim. Acta*, 2020, **334**, 135610.
7. T. Prasankumar, B. R. Wiston, C. Gautam, R. Ilangovan and S. P. Jose, *J. Alloys Compd*, 2018, **757**, 466-475.
8. J. Zhou, T. Qian, T. Yang, M. Wang, J. Guo and C. Yan, *J. Mater. Chem. A*, 2015, **3**, 15008-15014.
9. G. Li, J. Zhang, W. Li, K. Fan and C. Xu, *Nanoscale*, 2018, **10**, 9252-9260.
10. A. Kumar, D. Das, D. Sarkar, S. Patil and A. Shukla, *J. Electrochem. Soc.*, 2020, **167**, 060529.
11. J. Liu, X. Kang, X. He, P. Wei, Y. Wen and X. Li, *Nanoscale*, 2019, **11**, 9155-9162.
12. B. Tao, W. Yang, M. Zhou, L. Qiu, S. Lu, X. Wang, Q. Zhao, Q. Xie and Y. Ruan, *J Colloid Interface Sci.*, 2022, **621**, 139-148.
13. L. Li, F. Xie, H. Wu, Y. Zhu, P. Zhang, Y. Li, H. Li, L. Zhao and G. Zhu, *Molecules*, 2023, **28**, 5751.
14. N. M. Ndiaye, M. Madito, B. Ngom, T. Masikhwa, A. A. Mirghni and N. Manyala, *AIP Adv.*, 2019, **9**.
15. Y. Tan, Z. Xu, L. He and H. Li, *J. Energy Storage*, 2022, **52**, 104889.
16. D. Acharya, A. Muthurasu, T. H. Ko, R. M. Bhattarai, T. Kim, S.-H. Chae, S. Saidin, K. Chhetri and H. Y. Kim, *ACS Appl. Energy Mater.*, 2023, **6**, 9196-9206.
17. M. Chen, K. Yang, B. Dong, Q. Zhou, Y. Zhang, Y. Zhu, A. Iqbal, X. Liu, C. Yan and C. Low, *J. Power Sources*, 2023, **553**, 232272.
18. H. Shi, A. Zhang, X. Zhang, H. Yin, S. Wang, Y. Tang, Y. Zhou and P. Wu, *Nanoscale*, 2018, **10**, 4962-4968.
19. K. Roy, V. Chavan, S. M. Hossain, S. Haldar, R. Vaidhyanathan, P. Ghosh and S. B. Ogale, *ChemSusChem*, 2020, **13**, 196-204.
20. B. Cong, Y. Hu, S. Sun, Y. Wang, B. Wang, H. Kong and G. Chen, *Nanoscale*, 2020, **12**, 16901-16909.
21. J.-c. Zheng, Y.-y. Yao, G.-q. Mao, H.-z. Chen, H. Li, L. Cao, X. Ou, W.-j. Yu, Z.-y. Ding and H. Tong, *J. Mater. Chem. A*, 2019, **7**, 16479-16487.
22. W. Shen, W. Kou, Y. Liu, Y. Dai, W. Zheng, G. He, S. Wang, Y. Zhang, X. Wu and S. Fan, *Chem. Eng. J.*, 2019, **368**, 310-320.
23. A. Kitajou, S. Kudo, J.-i. Hayashi and S. Okada, *Electrochem.*, 2017, **85**, 630-633.

24.   H. Liu, S.-h. Luo, D.-b. Hu, X. Liu, Q. Wang, Z.-y. Wang, Y.-l. Wang, L.-j. Chang, Y.-g. Liu and T.-F. Yi, *Appl. Surf. Sci.*, 2019, **495**, 143590.